Engineering Structures 326 (2025) 119500

Contents lists available at ScienceDirect

Engineering Structures

journal homepage: www.elsevier.com/locate/engstruct

A coupled finite element–boundary element method for transient elastic dynamic analysis of electronic packaging structures

Yanpeng Gong [a,b], Yida He [a], Han Hu [b], Xiaoying Zhuang [b,c,*], Fei Qin [a], Hao Xu [a], Timon Rabczuk [d]

[a] Institute of Electronics Packaging Technology and Reliability, Department of Mechanics, Beijing University of Technology, 100124 Beijing, China
[b] Chair of Computational Science and Simulation Technology, Institute of Photonics, Department of Mathematics and Physics, Leibniz University Hannover, 30167 Hannover, Germany
[c] Department of Geotechnical Engineering, College of Civil Engineering, Tongji University, Shanghai, 200092, China
[d] Institute of Structural Mechanics, Bauhaus-Universität Weimar, 99423 Weimar, Germany

ARTICLE INFO

Keywords:
FE–BE coupling method
Transient elastodynamics problem
Electronic packaging
Abaqus implementation

ABSTRACT

Dynamic loading is a critical factor influencing the reliability of electronic packaging, necessitating the development of efficient and accurate numerical methods tailored for studying electronic packaging reliability. This paper presents a coupled finite element–boundary element approach suitable for analyzing transient elastic dynamic response problems in electronic packaging structures. The core concept involves integrating the boundary element method into the finite element framework, thereby reducing the number of elements required for the finite element analysis of intricate electronic packaging geometries. Additionally, to leverage the powerful pre-processing and post-processing capabilities offered by commercial finite element software, the boundary element method is integrated into Abaqus, forming a finite element–boundary element coupling algorithm within this platform. In the numerical analysis process, the structure under investigation is first partitioned into finite element and boundary element domains according to its geometric characteristics and material properties. These distinct domains are then modeled separately within Abaqus, where material properties and element types are assigned. Compared to traditional numerical analysis methodologies for electronic packaging structures, this coupled algorithm fully capitalizes on the robust pre-processing and secondary development capabilities of Abaqus, effectively combining the advantages of both the finite element and boundary element methods while reducing the number of elements required in the finite element analysis. Numerical examples demonstrate the efficacy of this coupled algorithm in analyzing dynamic problems prevalent in electronic packaging structures.

1. Introduction

More than 20% of electronic equipment failures are caused by dynamic loads, which are considered to be another major environmental factor causing electronic equipment failures besides thermal loads [1]. During the service life of electronic devices, packaging structures may suffer from fatigue damage and interface fractures due to dynamic loads, seriously threatening the long-term reliability of electronic packaging [2]. Therefore, a deep understanding and research into the dynamic response of packaging structures are of significant practical importance. Numerical simulation methods, which involve processing mathematical models on computers to simulate the actual behavior of systems, provide researchers with powerful tools to explore and understand the dynamic responses and behaviors of complex systems. In practical engineering, various numerical simulation methods can be employed to study dynamic problems. These include the finite element method (FEM) [3], boundary element method (BEM) [4], discrete element method (DEM) [4], meshfree methods (MMs) [5], and finite difference method (FDM) [6], among others. Recent studies have shown significant progress in dynamic analysis methods. Yahiaoui et al. combined the FEM with Saunders shell theory to conduct vibration analysis of geometrically defective plates under various boundary conditions [7]. Chen et al. [8] proposed a model order reduction method for electromagnetic boundary element analysis, ensuring geometric accuracy while avoiding remeshing during optimization. Barros

* Corresponding author at: Chair of Computational Science and Simulation Technology, Institute of Photonics, Department of Mathematics and Physics, Leibniz University Hannover, 30167 Hannover, Germany.
E-mail addresses: yanpeng.gong@bjut.edu.cn (Y. Gong), zhuang@iop.uni-hannover.de (X. Zhuang).

https://doi.org/10.1016/j.engstruct.2024.119500
Received 6 September 2024; Received in revised form 24 November 2024; Accepted 12 December 2024

et al. [4] developed a new multi-scale time-staggered coupling method of BEM and DEM to overcome limitations of previous approaches. Omar et al. [9] introduced an efficient meshless tool for dynamic analysis of functionally graded-reinforced composite beams under different boundary conditions. Jamali et al. [10] established a journal dynamic response model based on the Taguchi method, analyzing dynamic response under impact loads using finite difference method.

In the field of research on the reliability of electronic packaging structures, FEM is widely used to study the deformation and stress in electronic packaging caused by dynamic loads. Xia and collaborators [11] combined experimental testing with finite element simulation to study the vibration reliability and fatigue life prediction of Package on Package (POP) structures under vibrational loads. Kim and collaborators [12] conducted numerical simulations using the finite element method to study the reliability of PBGA packaging in a random vibration environment. Agwai and coauthors [13] combined the finite element method and peridynamic theory to predict the dynamic response and solder joint damage of electronic packaging structures under drop impact loads. Zhang and coauthors [14] used finite element analysis to obtain the modal parameters of board-level packaging and optimized the equivalent material properties, providing an effective tool for future finite element analysis of the dynamic response of board-level packaging and solder joints. Meanwhile, finite element commercial software has become the preferred tool in the field of engineering design and analysis due to its efficiency, accuracy, ease of use, good integration, modularity and scalability, as well as strong technical support and services. In Ref. [15], Chandana and coauthors used the finite element software Abaqus to conduct dynamic drop test analyses on Ball Grid Array (BGA) packaging, to evaluate the stress distribution in solder joints during a drop, and to analyze the drop reliability of electronic devices. In Ref. [16], Gong and coauthors used the ANSYS software platform to study the dynamic characteristics of the bonding head in a Flip Chip Bonder (FCB) under both static and dynamic constraints. In Ref. [17], Jia and collaborators proposed a multiphysics modeling approach based on PSpice and COMSOL to study the dynamic characteristics of IGBT power modules at different time scales.

While the finite element method offers flexibility and efficiency, it involves extensive computations, has a high dependence on the mesh, and encounters difficulties in handling complex boundary conditions as well as convergence issues. For certain intricate electronic packaging structures, generating high-quality finite element meshes poses a significant challenge, potentially compromising the accuracy and reliability of the computational results obtained. As an efficient numerical alternative, the boundary element method offers a significant reduction in computational complexity when compared to the finite element method. This advantage stems from the BEM requiring discretization solely at the boundary of the considered model, effectively reducing the degrees of freedom involved in the computations. By fully leveraging the information on the boundary, the BEM can enhance the accuracy of the analysis. These intrinsic characteristics render the boundary element method a powerful tool for analyzing multi-scale structures prevalent in electronic packaging applications. Tay and coauthors [18] developed a special variable-order singular boundary element method for the interface delamination issue in integrated circuit (IC) packaging, revealing the patterns of how defect size and location affect delamination. Khatir and collaborators [19] utilized the boundary element method to study the effects of thermal fatigue on IGBT modules. Their study revealed that the position of the IGBT chip on the DCB substrate significantly influences its lifespan. Optimizing the chip's location can effectively extend the operational lifetime of the module.

Dong and co-authors [20] employed the boundary element method for stress analysis of plastic integrated circuit packaging with various interfacial delaminations. By deriving fundamental solutions that leveraged the symmetry inherent to the problem, they were able to reduce the required number of boundary elements, thereby enhancing computational efficiency. In Ref. [21], Yu and collaborators utilized the isogeometric boundary element method (IGABEM) to address thermal analysis challenges in electronic packaging structures, offering strategies to accommodate internal heat sources and multi-material characteristics. However, the boundary element method also exhibits certain limitations in analyzing electronic packaging problems. These include numerous singular integrals during numerical computation, dense and asymmetric coefficient matrices, as well as difficulties in addressing nonlinear and non-homogeneous issues [22,23]. Furthermore, electronic packaging frequently involves three-dimensional problems, and the application of the boundary element method in such 3D contexts remains relatively limited, potentially necessitating further research efforts to expand its capabilities in this domain [24].

To fully capitalize on the strengths while mitigating the shortcomings of both the finite element method and the boundary element method, combining them to analyze problems can render the solution process more efficient. The coupling of finite elements and boundary elements was first proposed by Zienkiewicz and co-authors in 1977 [25]. Since its inception, this coupled approach combining finite element and boundary element methods has garnered significant attention from scholars and has been applied across various research domains. Overall, these coupling methodologies can be broadly categorized into two main strategies: incorporating the boundary element method into the finite element formulation, and conversely, integrating the finite element method into the boundary element framework [26]. Within the domain of electronic packaging, the application of these coupling methodologies to investigate pertinent issues has also witnessed notable advancements.

In Ref. [27], Guven and co-authors proposed a coupling algorithm that synergistically combined the BEM and FEM. This coupled BEM–FEM approach was tailored to efficiently and accurately solve transient 2D heat conduction problems prevalent in electronic packaging applications. Notably, it exhibited advantages in handling singularities in heat flux density stemming from material and geometric discontinuities. In Ref. [28], Das and co-authors proposed a coupling methodology that combined the boundary element method with the finite element method, leveraging the super element function available in the ANSYS software. This coupled BEM–FEM approach was employed to analyze the mechanical behavior of the functionally graded material (FGM) underfill layer present in electronic packaging under varying temperature conditions. In Refs. [29,30], Qin and co-authors utilized a coupling approach that integrated the finite element method with the boundary element method to investigate elastoplastic behavior and steady-state two-dimensional heat conduction in multiscale structures pertinent to electronic packaging applications. In [31,32], Chen et al. proposed coupled FEM–BEM methods for simulating acoustic–structure interactions and improving broadband topology optimization efficiency. This coupled FEM–BEM methodology significantly reduced computational time requirements while concurrently enhancing the accuracy of the obtained solutions. Meanwhile, these coupled methodologies integrating finite element and boundary element approaches have also found applications in the investigation of dynamic problems [33–35].

Numerous commercial finite element software packages boast powerful pre-processing and post-processing capabilities. Among them, Abaqus offers a comprehensive library of elements and material models, coupled with robust and flexible user subroutines. The provided secondary development interface enables users to define any complex element formulations tailored to their specific problem requirements [36]. In this paper, we analyze the transient elastic dynamic response of electronic packaging structures by coupling the BEM with the FEM utilizing the finite element software Abaqus. Based on the geometric characteristics or material properties, the model is partitioned into finite element domains and boundary element domains. The finite element domains, solved via the FEM in Abaqus, typically encompass smaller structures exhibiting nonlinear and heterogeneous material behavior. Conversely, larger structures with linear material properties

are defined as boundary element domains and analyzed using a self-written planar transient elastic dynamics boundary element program. The boundary element domain is treated as a specialized finite element. Through the user-defined element subroutine (UEL) in Abaqus, the boundary element program is invoked to obtain the equivalent stiffness matrix and equivalent load vector for the boundary element domain. These are subsequently assembled with the finite element domain to form the global system matrix, which is then provided to Abaqus for computing the physical quantities within the finite element domain. The URDFIL subroutine is employed to extract the computational results at the coupling interface between the finite element and boundary element domains. The term 'coupling interface' in this work is equivalent to the commonly used 'contact interface'. These extracted results serve as known boundary conditions for the boundary element program to solve the boundary element domain, ultimately completing the solution for the entire computational domain.

The content of this paper is organized as follows: Section 2 provides an introduction to dynamic problems and their treatment using the FEM and BEM. Section 3 outlines the finite element–boundary element coupling algorithm employed in this work. Section 4 demonstrates the application of the proposed coupling algorithm through numerical examples, analyzing the dynamic response of various electronic packaging structures. Finally, relevant conclusions are presented in Section 5.

2. Governing equations for transient elastodynamic problems

This section briefly outlines the fundamental theoretical underpinnings of the FEM and the BEM as applied to transient elastodynamic response problems.

2.1. Fundamental finite element formulations for elastodynamics

The construction of finite elements for dynamics problems in finite element analysis follows a similar process to that of static problems, encompassing element selection, definition of shape functions, and the assembly of local and global stiffness matrices. However, a key distinction between dynamic and static analyses lies in the additional considerations required to account for time-varying factors and the treatment of inertial and damping forces. For dynamics problems, the system's response is influenced not only by external loads but also by the system's intrinsic inertial and damping forces. Consequently, the fundamental equation for dynamics problems in the FEM is derived from the principle of dynamic virtual work. For linear systems, this virtual work equation is typically expressed as:

$$\delta W = \delta W_{\text{ext}} - \delta W_{\text{int}} = 0 \tag{1}$$

where δW_{ext} is the external virtual work, represented by the work done by external loads on virtual displacements. δW_{int} denotes the internal virtual work, which encompasses the virtual work produced by stresses, virtual work arising from structural damping, and virtual work due to structural inertia forces.

For systems involving inertial and damping effects, the expression for internal virtual work can be expanded as follows:

$$\delta W_{\text{int}} = \int_V \sigma : \delta\epsilon \, dV + \int_V c\dot{u} \cdot \delta\dot{u} \, dV + \int_V \rho\ddot{u} \cdot \delta u \, dV \tag{2}$$

Here, σ is the stress tensor; $\delta\epsilon$ is the virtual strain; c is the damping coefficient; $\dot{u}$ and $\delta\dot{u}$ are the velocity and virtual velocity, respectively. ρ is the material density; ü and δu are the acceleration and virtual displacement, respectively. V is the volume of the structure.

Employing the Einstein summation convention, for dynamic problems that consider inertial and damping effects, the virtual work principle takes the following form [25]:

$$\int_V \left(D_{ijkl}\epsilon_{ij}\delta\epsilon_{kl} + \rho\ddot{u}_i\delta u_i + c\dot{u}_i\delta u_i \right) \mathrm{d}V - \left(\int_V b_i\delta u_i \mathrm{d}V + \int_S p_i\delta u_i \mathrm{d}A \right) = 0 \tag{3}$$

where D_{ijkl} denotes the elasticity coefficient matrix. b_i and p_i are the components of body and traction forces, respectively, with body forces acting throughout the material's volume and traction forces applied across its boundaries.

The displacement $\mathbf{u}(\mathbf{x})$ at any point $\mathbf{x}$ within the element e can be expressed as a linear combination of the shape functions and the nodal displacements u_i of the element. The general form of the interpolation function is given by:

$$\mathbf{u}^e(\mathbf{x}) = \sum_{i=1}^{n} N_i(\mathbf{x}) u_i^e \tag{4}$$

where N_i is the shape function associated with the i-th node, u_i^e is the displacement at the i-th node of element e, n is the number of nodes in the element.

Based on Eq. (4) and the governing geometric and constitutive relations, the strain, stress, velocity, and acceleration fields can be expressed in terms of the nodal displacements. These expressions are subsequently substituted into the virtual work Eq. (3). Then, we obtain

$$\delta W = \left[\mathbf{M}^e\ddot{\mathbf{u}}^e(t) + \mathbf{C}^e\dot{\mathbf{u}}^e(t) + \mathbf{K}^e\mathbf{u}^e(t) - \mathbf{P}^e(t) \right]^{\mathrm{T}} \delta\mathbf{u}^e(t) = 0 \tag{5}$$

Since $\delta W = 0$ must hold for any arbitrary variation $\delta\mathbf{u}^e$, the equation simplifies to:

$$\mathbf{M}^e\ddot{\mathbf{u}}^e(t) + \mathbf{C}^e\dot{\mathbf{u}}^e(t) + \mathbf{K}^e\mathbf{u}^e(t) = \mathbf{P}^e(t) \tag{6}$$

where

$$\mathbf{M}^e = \int_{V^e} \rho\mathbf{N}^{\mathrm{T}}\mathbf{N} dV \tag{7}$$

$$\mathbf{C}^e = \int_{V^e} c\mathbf{N}^{\mathrm{T}}\mathbf{N} dV \tag{8}$$

$$\mathbf{K}^e = \int_{V^e} \mathbf{B}^{\mathrm{T}}\mathbf{D}\mathbf{B} dV \tag{9}$$

$$\mathbf{P}^e = \int_{V^e} \mathbf{N}^{\mathrm{T}}\mathbf{b} dV + \int_{S^e} \mathbf{N}^{\mathrm{T}}\mathbf{p} dA \tag{10}$$

Finally, assembling the element matrices yields the following matrix form of the finite element equations:

$$\mathbf{M}\ddot{\mathbf{u}} + \mathbf{C}\dot{\mathbf{u}} + \mathbf{K}\mathbf{u} = \mathbf{P}(t) \tag{11}$$

$\mathbf{M}$ represents the global mass matrix, $\mathbf{C}$ denotes the global damping matrix, and $\mathbf{K}$ is the global stiffness matrix. $\mathbf{P}(t)$ is the external force vector. In cases where inertial and damping forces are neglected, Eq. (11) simplifies to the conventional finite element equation for static problems.

In this work, the system of equations is solved using the Abaqus solver, which employs numerical techniques tailored for dynamic response analysis, such as the Hilber–Hughes–Taylor (HHT) implicit algorithm and the Newton–Raphson iterative method. These methods are based on the principles of the Newmark integration technique, with the iterative formula for computing the dynamic response given by:

$$\tilde{\mathbf{K}}_{n+1}\mathbf{u}(t+\Delta t) = \tilde{\mathbf{F}}_{n+1} \tag{12}$$

$$\mathbf{u}(t+\Delta t) = \mathbf{u}(t) + \Delta t\dot{\mathbf{u}}(t) + \left(\frac{1}{2} - \beta\right)\Delta t^2\ddot{\mathbf{u}}(t) + \beta\Delta t^2\ddot{\mathbf{u}}(t+\Delta t) \tag{13}$$

$$\dot{\mathbf{u}}(t+\Delta t) = \dot{\mathbf{u}}(t) + (1-\gamma)\Delta t\ddot{\mathbf{u}}(t) + \gamma\Delta t\ddot{\mathbf{u}}(t+\Delta t) \tag{14}$$

The expression for the effective stiffness matrix and effective load vector can be written as:

$$\tilde{\mathbf{K}}_{n+1} = \mathbf{K} + \frac{1}{\beta\Delta t^2}\mathbf{M} + \frac{\gamma}{\beta\Delta t}\mathbf{C} \tag{15}$$

and

$$\tilde{\mathbf{F}}_{n+1} = \mathbf{P}_{n+1} + \frac{1}{\beta \Delta t^2}(\mathbf{M} + \mathbf{C}\gamma \Delta t)\left[\mathbf{u}_n + \Delta t \dot{\mathbf{u}}_n + \left(\frac{1}{2} - \beta\right)\Delta t^2 \ddot{\mathbf{u}}_n\right] - \mathbf{C}\left[\dot{\mathbf{u}}_n + (1-\gamma)\Delta t \ddot{\mathbf{u}}_n\right] \tag{16}$$

where

$$\beta = \frac{1}{4}(1-\alpha)^2$$

$$\gamma = \frac{1}{2} - \alpha$$

and $\alpha \in (-1/3, 0)$. When the parameter α is set to zero, the numerical damping inherently introduced by the method effectively vanishes, simplifying the integration scheme to the traditional Newmark method.

2.2. Boundary element formulations for dynamic problems

For small deformations in a homogeneous, isotropic elastic body, the governing dynamic equilibrium equation can be expressed as:

$$(\lambda + 2G)\nabla\nabla \cdot \mathbf{u} - G\nabla \times \nabla \times \mathbf{u} - \rho\frac{\partial^2 \mathbf{u}}{\partial t^2} + \rho\mathbf{b} = 0 \tag{17}$$

where $\mathbf{b}$ represents the body force vector, and $\mathbf{u}$ denotes the displacement vector. The shear modulus G and the coefficient λ satisfy the relationship:

$$G = \frac{E}{2(1+\upsilon)}$$

$$\lambda = \frac{\upsilon E}{(1+\upsilon)(1-2\upsilon)}$$

where E is the modulus of elasticity and υ is the Poisson's ratio.

When analyzing the dynamic response of an elastic body, introducing simplifying assumptions can often facilitate analytical or numerical solutions. Neglecting body forces ($\rho\mathbf{b} = 0$) and imposing zero initial conditions for displacement ($\mathbf{u}_0 = 0$) and velocity ($\mathbf{v}_0 = 0$) significantly simplify the governing equations and the subsequent analysis. Under these assumptions, the dynamic behavior of a two-dimensional elastic body can be represented through integral equations in both the time and spatial domains, expressed as [37]:

$$c_{lk}^i u_k^i(\mathbf{x}^i, t) = \int_0^{t^+}\int_\Gamma u_{lk}^*(\mathbf{x}, t-\tau; \mathbf{x}^i) p_k(\mathbf{x}, \tau) d\Gamma(\mathbf{x}) d\tau - \int_0^{t^+}\int_\Gamma p_{lk}^*(\mathbf{x}, t-\tau; \mathbf{x}^i) u_k(\mathbf{x}, \tau) d\Gamma(\mathbf{x}) d\tau \tag{18}$$

where $l, k = 1, 2$, $\mathbf{x}^i$ denotes the ith source point and $\mathbf{x}$ represents the field point. c_{lk}^i is a constant value related to the boundary geometry at the source point $\mathbf{x}^i$, with $c_{lk}^i = 1/2\delta_{lk}$ when $\mathbf{x}^i$ lies on a smooth boundary. $u_k^i(\mathbf{x}^i, t)$ is the displacement value at the source $\mathbf{x}^i$. τ represents the instant when the unit impulse load is applied at the source point $\mathbf{x}^i$, while t denotes the moment when quantities such as displacement and traction are measured at the field point. $u_k(\mathbf{x}, \tau)$ and $t_k(\mathbf{x}, \tau)$ represent the displacement and traction components, respectively, of the point $\mathbf{x}$ on the boundary Γ at time τ. The displacement fundamental solution u_{lk}^* and traction fundamental solution p_{lk}^* are referred in Ref. [37].

The discretization process plays a pivotal role in solving boundary integral equation problems, as it transforms the continuous problem into a discrete system amenable to numerical solution techniques. Assuming the boundary Γ is discretized into N_e elements, with a total of N nodes, and the time domain is uniformly divided into n time steps of length Δt, the discrete form of the boundary integral equation can be represented as:

$$c_{lk}^i u_k^{ni} = \sum_{m=1}^{n}\sum_{j=1}^{N}\left(\left[\int_{\Gamma_j} U_{lk}^{nm}\Psi^j d\Gamma\right] p_k^{mj} - \left[\int_{\Gamma_j} P_{lk}^{nm}\Phi^j d\Gamma\right] u_k^{mj}\right) \tag{19}$$

where u_k^{mj} and p_k^{mj} represent the displacement and traction at boundary node j at time t_m ($t_m = m\Delta t$), respectively. Set

$$G_{lk}^{nmij} = \int_{\Gamma_j} U_{lk}^{nm}\Psi^j d\Gamma \tag{20}$$

and

$$\hat{H}_{lk}^{nmij} = \int_{\Gamma_j} P_{lk}^{nm}\Phi^j d\Gamma, \tag{21}$$

the discrete BIE in Eq. (19) can be written as

$$c_{lk}^i u_k^{ni} = \sum_{m=1}^{n}\sum_{j=1}^{N}\left(G_{lk}^{nmij} p_k^{mj} - \hat{H}_{lk}^{nmij} u_k^{mj}\right) \tag{22}$$

Let

$$H_{lk}^{nmij} = \begin{cases} \hat{H}_{lk}^{nmij}, & (i \neq j \text{ or } n \neq m) \\ \hat{H}_{lk}^{nmij} + c_{lk}^i, & (i = j \text{ and } n = m) \end{cases} \tag{23}$$

the Eq. (22) can be written as

$$\sum_{m=1}^{n}\sum_{j=1}^{N} H_{lk}^{nmij} u_k^{mj} = \sum_{m=1}^{n}\sum_{j=1}^{N} G_{lk}^{nmij} p_k^{mj} \tag{24}$$

For the sake of brevity, the boundary integral equation can be compactly represented in the following matrix form:

$$\sum_{m=1}^{n} \mathbf{H}^{nm}\mathbf{u}^m = \sum_{m=1}^{n} \mathbf{G}^{nm}\mathbf{p}^m \tag{25}$$

In this expression, $\mathbf{u}^m$ and $\mathbf{p}^m$ comprise the displacement and traction values at each node for the mth time step, respectively. The components H_{lk}^{nmij} and G_{lk}^{nmij} of the matrices $\mathbf{H}^{nm}$ and $\mathbf{G}^{nm}$ are obtained through the corresponding integrals. By applying suitable transformations, this system of equations can be converted into the following form:

$$\mathbf{H}^{nn}\mathbf{u}^n = \mathbf{G}^{nn}\mathbf{p}^n + \sum_{m=1}^{n-1}\left[\mathbf{G}^{nm}\mathbf{p}^m - \mathbf{H}^{nm}\mathbf{u}^m\right] \tag{26}$$

In the computational procedure, this system of equations is solved sequentially, commencing with $m = 1$ and progressing through each time step up to n. The values to be determined at each time step n depend on the values of $\mathbf{u}^m$ and $\mathbf{t}^m$ (for $m = 1, 2, \ldots, n-1$) from all preceding steps. Consequently, the matrices derived from each computation are stored to enable their reuse in subsequent time steps.

2.3. Coupled finite element–boundary element method scheme

This section introduces the fundamental principles underpinning the Finite element–boundary Element (FE–BE) coupling scheme, which falls under the category of equivalent FEM. Consider an isotropic, homogeneous continuum subjected to external forces. This structure is partitioned into finite element and boundary element domains, denoted as Ω^F and Ω^B, respectively. The division of regions and the discretization of the model are illustrated in Figs. 1(a) and 1(b). Notably, the boundary element domain is treated as a specialized type of finite element, referred to as an equivalent boundary element.

To effectively couple the BEM with the FEM, it is essential to separate the interface variables from the non-interface variables within the finite element domain. Referring to the node positions illustrated in Fig. 1(b), the stiffness equation for the finite element domain can be expanded and restructured as follows:

$$\begin{bmatrix} K_1^1 & \cdots & K_1^N & K_1^g & \cdots & K_1^h \\ \vdots & \ddots & \vdots & \vdots & \ddots & \vdots \\ K_N^1 & \cdots & K_N^N & K_N^g & \cdots & K_N^h \end{bmatrix} \times \begin{Bmatrix} u_1 \\ \vdots \\ u_N \\ u_g \\ \vdots \\ u_h \end{Bmatrix} = \begin{Bmatrix} F_1 \\ \vdots \\ F_N \\ F_g \\ \vdots \\ F_h \end{Bmatrix} \tag{27}$$

After reorganizing the equations by separating the stiffness matrix contributions from the internal nodes and the coupling interface nodes, the resulting system can be expressed in the following matrix form:

$$\begin{bmatrix} \mathbf{K}_{oo} & \mathbf{K}_{oi} \\ \mathbf{K}_{io} & \mathbf{K}_{ii} \end{bmatrix} \begin{Bmatrix} \mathbf{u}_{Fo}^{n+1} \\ \mathbf{u}_{Fi}^{n+1} \end{Bmatrix} = \begin{Bmatrix} \mathbf{F}_{Fo}^{n+1} \\ \mathbf{F}_{Fi}^{n+1} \end{Bmatrix} \tag{28}$$

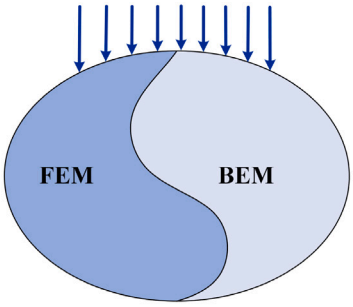

(a) Model with FE domain (Ω^F) and BE domain (Ω^B).

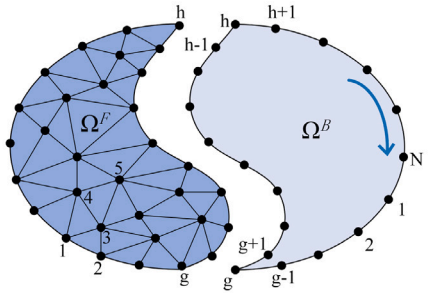

(b) Schematic of model discretization.

Fig. 1. Coupled BEM–FEM model.

In this matrix form, the subscripts '*Fi*' and '*Fo*' denote the physical quantities at the contact interface and non-interface regions within the finite element domain, respectively. The matrices $\mathbf{K}$ and vectors $\mathbf{F}$ are obtained by reorganizing the existing matrices $\tilde{\mathbf{K}}$ and vectors $\tilde{\mathbf{F}}$ from the previously uncoupled formulation given in Eq. (12).

To compute the coefficients populating the matrix $\mathbf{K}$ and vector $\mathbf{F}$ utilized in Eq. (28), specific computational strategies are necessary. The following outlines a detailed approach for evaluating these coefficients:

$$\begin{bmatrix} \mathbf{K}_{oo} & \mathbf{K}_{oi} \\ \mathbf{K}_{io} & \mathbf{K}_{ii} \end{bmatrix} = \begin{bmatrix} \tilde{\mathbf{K}}_{oo} + a_0\mathbf{M}_{oo} & \tilde{\mathbf{K}}_{oi} + a_0\mathbf{M}_{oi} \\ \tilde{\mathbf{K}}_{io} + a_0\mathbf{M}_{io} & \tilde{\mathbf{K}}_{ii} + a_0\mathbf{M}_{ii} \end{bmatrix} \tag{29}$$

$$\begin{Bmatrix} \mathbf{F}_{Fo}^{n+1} \\ \mathbf{F}_{Fi}^{n+1} \end{Bmatrix} = \begin{Bmatrix} \mathbf{P}_{Fo}^{n+1} \\ \mathbf{P}_{Fi}^{n+1} \end{Bmatrix} + \begin{bmatrix} \mathbf{M}_{oo} & \mathbf{M}_{oi} \\ \mathbf{M}_{io} & \mathbf{M}_{ii} \end{bmatrix} \begin{Bmatrix} \mathbf{f}_{Fo}^{n} \\ \mathbf{f}_{Fi}^{n} \end{Bmatrix} \tag{30}$$

where

$$\begin{Bmatrix} \mathbf{f}_{Fo}^{n} \\ \mathbf{f}_{Fi}^{n} \end{Bmatrix} = \begin{Bmatrix} a_0\mathbf{u}_{Fo}^{n} + a_1\dot{\mathbf{u}}_{Fo}^{n} + a_2\ddot{\mathbf{u}}_{Fo}^{n} \\ a_0\mathbf{u}_{Fi}^{n} + a_1\dot{\mathbf{u}}_{Fi}^{n} + a_2\ddot{\mathbf{u}}_{Fi}^{n} \end{Bmatrix} \tag{31}$$

$$a_0 = \frac{1}{\beta\Delta t^2},\ a_1 = \frac{1}{\beta\Delta t},\ a_2 = \frac{1}{2\beta} - 1 \tag{32}$$

Similarly, Eq. (26) can be written in the matrix form:

$$\begin{bmatrix} \mathbf{H}_{ii} & \mathbf{H}_{io} \\ \mathbf{H}_{oi} & \mathbf{H}_{oo} \end{bmatrix} \begin{Bmatrix} \mathbf{u}_{Bi}^{n+1} \\ \mathbf{u}_{Bo}^{n+1} \end{Bmatrix} = \begin{bmatrix} \mathbf{G}_{ii} & \mathbf{G}_{io} \\ \mathbf{G}_{oi} & \mathbf{G}_{oo} \end{bmatrix} \begin{Bmatrix} \mathbf{p}_{Bi}^{n+1} \\ \mathbf{p}_{Bo}^{n+1} \end{Bmatrix} + \begin{Bmatrix} \mathbf{r}_{Bi}^{n} \\ \mathbf{r}_{Bo}^{n} \end{Bmatrix} \tag{33}$$

$$\begin{Bmatrix} \mathbf{r}_{Bi}^{n} \\ \mathbf{r}_{Bo}^{n} \end{Bmatrix} = \sum_{\mathrm{m}=1}^{\mathrm{n}} [\mathbf{G}^{nm}\mathbf{p}^{m} - \mathbf{H}^{nm}\mathbf{u}^{m}] \tag{34}$$

where the subscript *Bi* denotes variables situated at the contact interface between the boundary element domain and the finite element domain, while *Bo* refers to boundary variables that do not directly interact with the finite element region.

To make $\mathbf{H}_{io} = 0$ in Eq. (33), applying Gaussian elimination enables us to obtain

$$\begin{bmatrix} \mathbf{C}_{ii} & \mathbf{0} \\ \mathbf{C}_{oi} & \mathbf{C}_{oo} \end{bmatrix} \begin{Bmatrix} \mathbf{u}_{Bi}^{n+1} \\ \mathbf{u}_{Bo}^{n+1} \end{Bmatrix} = \begin{bmatrix} \mathbf{D}_{ii} & \mathbf{D}_{io} \\ \mathbf{D}_{oi} & \mathbf{D}_{oo} \end{bmatrix} \begin{Bmatrix} \mathbf{p}_{Bi}^{n+1} \\ \mathbf{p}_{Bo}^{n+1} \end{Bmatrix} + \begin{Bmatrix} \widehat{\mathbf{r}}_{Bi}^{n} \\ \widehat{\mathbf{r}}_{Bo}^{n} \end{Bmatrix} \tag{35}$$

Then, we can derive the relationship between the nodal displacements and the tractions at the interface

$$\mathbf{C}_{ii}\mathbf{u}_{Bi}^{n+1} = \mathbf{D}_{ii}\mathbf{p}_{Bi}^{n+1} + \mathbf{D}_{io}\mathbf{p}_{Bo}^{n+1} + \widehat{\mathbf{r}}_{Bi}^{n} \tag{36}$$

By multiplying both sides of Eq. (36) by the inverse of the matrix $\mathbf{D}_{ii}$ and performing suitable rearrangements, the following expression can be derived, relating the surface force components to the displacement components at the interface.

$$\mathbf{p}_{Bi}^{n+1} = \mathbf{D}_{ii}{}^{-1}\mathbf{C}_{ii}\mathbf{u}_{Bi}^{n+1} - \mathbf{D}_{ii}{}^{-1}\mathbf{D}_{io}\mathbf{p}_{Bo}^{n+1} - \mathbf{D}_{ii}{}^{-1}\widehat{\mathbf{r}}_{Bi}^{n} \tag{37}$$

Similar to the static coupling algorithm, the physical quantities described by the BEM are nodal tractions and displacements, while the FEM characterizes these using equivalent nodal forces and displacements. The coupling strategy adopted in this work involves integrating the BEM into the finite element framework. Consequently, it becomes necessary to convert the nodal tractions $\mathbf{p}_{Bi}^{n+1}$ into their equivalent nodal force representations $\mathbf{F}_{Bi}^{n+1}$, with the transformation being expressed as:

$$\mathbf{F}_{Bi}^{n+1} = \mathbf{M}_B\mathbf{p}_{Bi}^{n+1} \tag{38}$$

By substituting Eq. (37) into Eq. (38), we can obtain

$$\mathbf{F}_{Bi}^{n+1} = \mathbf{M}_B\mathbf{D}_{ii}{}^{-1}\mathbf{C}_{ii}\mathbf{u}_{Bi}^{n+1} - \mathbf{M}_B\mathbf{D}_{ii}{}^{-1}\left(\mathbf{D}_{io}\mathbf{p}_{Bo}^{n+1} + \widehat{\mathbf{r}}_{Bi}^{n}\right) = \mathbf{K}_{Bi}^{n+1}\mathbf{u}_{Bi}^{n+1} - \bar{\mathbf{F}}_{Bi}^{n+1} \tag{39}$$

$\mathbf{M}_B$ represents the transformation matrix, $\mathbf{K}_{Bi}^{n+1}$ is the equivalent stiffness matrix of the boundary element domain, and $\bar{\mathbf{F}}_{Bi}^{n+1}$ is the equivalent load vector of the boundary element domain. Eq. (39) can be written as

$$\begin{bmatrix} 0 & 0 \\ 0 & \mathbf{K}_{Bi}^{n+1} \end{bmatrix} \begin{Bmatrix} \mathbf{u}_{Fo}^{n+1} \\ \mathbf{u}_{Bi}^{n+1} \end{Bmatrix} = \begin{Bmatrix} 0 \\ \mathbf{F}_{Bi}^{n+1} + \bar{\mathbf{F}}_{Bi}^{n+1} \end{Bmatrix} \tag{40}$$

Imposing the compatibility conditions along the contact interface between the finite element and boundary element domains, we have:

$$\begin{cases} \mathbf{u}_{Fi}^{n+1} = \mathbf{u}_{Bi}^{n+1} \\ \mathbf{P}_{Fi}^{n+1} = -\mathbf{F}_{Bi}^{n+1} \end{cases} \tag{41}$$

and combining Eqs. (28), (30), and (40), the finite element–boundary element equations can be derived as follows:

$$\begin{bmatrix} \mathbf{K}_{oo} & \mathbf{K}_{oi} \\ \mathbf{K}_{io} & \mathbf{K}_{ii} + \mathbf{K}_{Bi}^{n+1} \end{bmatrix} \begin{Bmatrix} \mathbf{u}_{Fo}^{n+1} \\ \mathbf{u}_{Fi}^{n+1} \end{Bmatrix} = \begin{Bmatrix} \mathbf{P}_{Fo}^{n+1} \\ \bar{\mathbf{F}}_{Bi}^{n+1} \end{Bmatrix} + \begin{bmatrix} \mathbf{M}_{oo} & \mathbf{M}_{oi} \\ \mathbf{M}_{io} & \mathbf{M}_{ii} \end{bmatrix} \begin{Bmatrix} \mathbf{f}_{Fo}^{n} \\ \mathbf{f}_{Fi}^{n} \end{Bmatrix} \tag{42}$$

It is worth noting that the matrix $\mathbf{K}_{Bi}^{n+1}$ is a full, asymmetric matrix, disrupting the symmetric and sparse banded structure typically exhibited by the finite element stiffness matrix. To address this, it becomes necessary to symmetrize the matrix $\mathbf{K}_{Bi}^{n+1}$. Thus, we can replace this matrix with the symmetric counterpart $\mathbf{K}_{l}^{n+1}$, where:

$$\mathbf{K}_{l}^{n+1} = \frac{1}{2}\left[\left(\mathbf{K}_{Bi}^{n+1}\right)^T + \mathbf{K}_{Bi}^{n+1}\right] \tag{43}$$

While matrix symmetrization here makes the formulation more elegant, it is worth noting that symmetric matrices were primarily required by early solvers. Modern commercial FEM software includes various robust solvers capable of handling non-symmetric matrices efficiently. To solve Eq. (42) directly without symmetrization, users only need to add the statement '*USER ELEMENT, LINEAR, NODES = n, UNSYMM' in the INP file.

The final form of the coupled equation is as follows:

$$\begin{bmatrix} \mathbf{K}_{oo} & \mathbf{K}_{oi} \\ \mathbf{K}_{io}\mathbf{K}_{ii}+\mathbf{K}_{I}^{n+1} \end{bmatrix} \begin{Bmatrix} \mathbf{u}_{Fo}^{n+1} \\ \mathbf{u}_{Fi}^{n+1} \end{Bmatrix} = \begin{Bmatrix} \mathbf{P}_{Fo}^{n+1} \\ \bar{\mathbf{F}}_{Bi}^{n+1} \end{Bmatrix} + \begin{bmatrix} \mathbf{M}_{oo}\mathbf{M}_{oi} \\ \mathbf{M}_{io}\mathbf{M}_{ii} \end{bmatrix} \begin{Bmatrix} \mathbf{f}_{Fo}^{n} \\ \mathbf{f}_{Fi}^{n} \end{Bmatrix} + \begin{Bmatrix} \mathbf{0} \\ \mathbf{K}_{I}^{n+1}-\mathbf{K}_{Bi}^{n+1} \end{Bmatrix} \left\{ \mathbf{u}_{Fi}^{n} \right\} \tag{44}$$

By solving the coupled system of equations, all the unknown quantities within the finite element domain can be determined, including the physical variables at the contact interface. Utilizing the displacements and surface tractions along the interface between the two regions as boundary conditions, the boundary physical quantities pertaining to the boundary element domain can be obtained by solving the boundary integral equation. After acquiring the displacement values $\mathbf{u}^n$ at the boundary nodes for each time step, the displacement field at any internal point $\mathbf{y}$ within the boundary element domain at time t can be evaluated through the following internal point boundary integral equation

$$\begin{aligned} u_l(\mathbf{y},t) = &\int_0^{t^+}\int_\Gamma u_{lk}^*(\mathbf{y},t-\tau;\mathbf{y})p_k(\mathbf{y},\tau)d\Gamma d\tau \\ &- \int_0^{t^+}\int_\Gamma p_{lk}^*(\mathbf{y},t-\tau;\mathbf{y})u_k(\mathbf{y},\tau)d\Gamma d\tau \end{aligned} \tag{45}$$

The displacement $\mathbf{u}^n$ at time $t_n = n\Delta t$ can be computed once the boundary nodal displacements at times $t = \Delta t, 2\Delta t, \ldots, n\Delta t$ are known. The displacement at any point $\mathbf{y}^i$ within the BE domain is obtained through the internal point Eq. (45), discretized similarly to the boundary integral equation in Section 2.2

$$u_l^{ni} = \sum_{m=1}^{n}\sum_{j=1}^{N}\left(G_{lk}^{nmij}p_k^{mj} - \hat{H}_{lk}^{nmij}u_k^{mj}\right) \tag{46}$$

where coefficients G_{lk}^{nmij} and $\hat{H}_{lk}^{nmij}$ are numerically computed for each internal point. Note that these coefficients depend on internal point i, boundary node j, and time difference $t_n - t_m$. This equation is solved incrementally for each time step, where values at the current time step t_n depend on p_k^{mj} and u_k^{mj} from all previous time steps t_m $(m = 1, 2, \ldots, n-1)$. At each new step n, only the term with maximum difference $n-1$ needs to be computed, as other terms are known from previous steps.

3. Implementation of the coupling algorithm within the Abaqus environment

Abaqus has powerful pre- and post-processing capabilities, as well as a fully featured secondary development platform. Its user-defined element subroutine (UEL) provides users with a convenient and open program interface, allowing users to customize elements according to specific engineering problems. This paper integrates the BEM into the Abaqus through the UEL subroutine interface, treating the boundary element domain as a type of special finite element integrated into the finite element model. Fig. 2 provides the technical route for implementing the coupling scheme, with the specific implementation process as follows:

3.1. Establishment of the initial coupling model

As shown in Fig. 1, the computational model is split into two sections: finite elements and boundary elements. The physical quantities for the finite element section are computed using Abaqus, whereas those for the boundary element section are calculated through a custom-written 'Plane Transient Elastic Dynamics Boundary Element Program'. Both sections are discretized using their respective methods: the FEM and the BEM. Notably, to ensure smooth application of

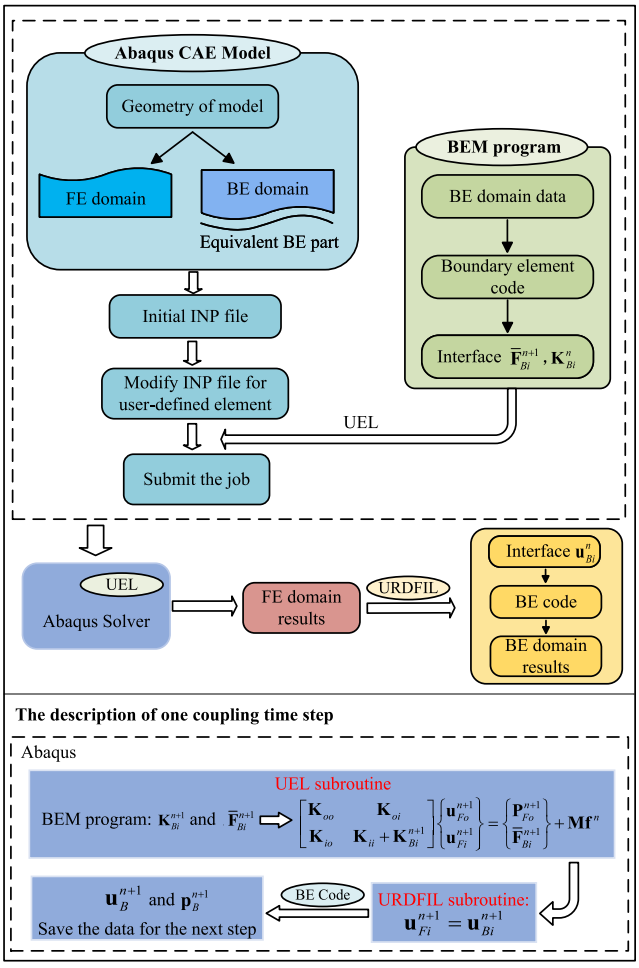

Fig. 2. Finite element–boundary element coupling algorithm based on Abaqus.

interface coordination conditions, this article maintains a consistent number of nodes at the contact interface between the two sections.

Based on this modeling approach, the initial geometric model is established in the Abaqus environment. The FE subdomain is created according to the actual geometric shape, while an equivalent BE component, representing the BE subdomain, is created coincident with the contact interface. The construction of the coupled model in Abaqus is similar to traditional FE modeling, including assigning material properties to both components, assembly, applying boundary conditions, and mesh discretization. The equivalent BE component is treated as a super-element in the INP file, where the number and coordinates of its nodes correspond one-to-one with the nodes at the contact interface of the FE subdomain, satisfying interface continuity conditions. Finally, the two parts are connected and assembled using the 'tie' command in Abaqus, as shown in Fig. 3. After completing the entire modeling process, the INP file containing the model is exported.

3.2. INP file modification and algorithm implementation

The INP file exported through the above operations contains all the data of the initial coupling model. However, since the equivalent boundary element part only includes the geometric information at the contact interface of the boundary element domain, it does not reflect the physical characteristics and boundary conditions at the non-coupling interfaces of the boundary element domain, and therefore cannot be directly used for problem solving. Therefore, we need to modify the element properties of the equivalent boundary element part

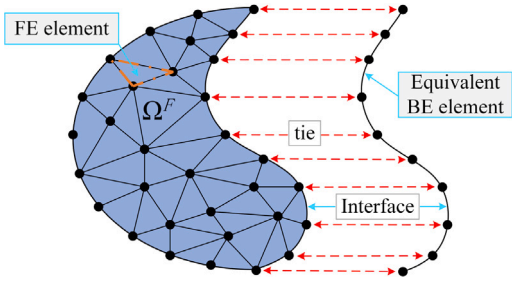

Fig. 3. Relationship of elements and nodes at the contact interface in the coupled model.

in the original INP file to user-defined elements (*USER ELEMENT), meaning that the boundary element part is treated as a special finite element. As is shown in Fig. 3, the number of nodes in the user-defined elements is consistent with the number of nodes on the contact interface. Then, submit the modified INP file to Abaqus and implement the coupling analysis with the BEM by calling the self-written boundary element program through the UEL subroutine.

The kernel of the algorithm is to obtain the equivalent stiffness matrix and equivalent load vector of the user-defined elements at the contact interface of the boundary element domain through the self-written 'Transient Elastic Dynamics Boundary Element Program'. These equivalent matrices are then coupled and assembled with the finite element part matrices to form the system's stiffness matrix and load vector, making the finite element part a solvable problem. Then, using Abaqus, all physical quantities of the finite element part (including the contact interface) are calculated, followed by the extraction of displacement values at the coupling interface using the subroutine URDFIL, which are then provided as known quantities to the boundary element program to calculate all physical quantities of the entire boundary element part.

Fig. 2 shows the coupling process within a single time step: The UEL subroutine calls the boundary element program to obtain the equivalent stiffness and equivalent loads of the boundary element domain, which are then provided to the main Abaqus program for solving. Subsequently, the interface displacement and surface force values are read through the subroutine URDFIL and returned to the boundary element program, which computes the displacement and traction forces on the boundary of the boundary element part, used for solving in the next time step.

4. Numerical examples

In this section, through several numerical examples, the accuracy and effectiveness of the coupled scheme using the Abaqus for electronic packaging structures are demonstrated. It should be noted that all examples in this section are based on elastic material properties. The elastoplastic constitutive model is crucial for ensuring mechanical reliability of electronic packaging structures under various dynamic scenarios [38,39]. Long et al. [40] proposed an Anand model framework that describes the plastic behavior of solder materials across wide temperature and strain rate ranges. Wang et al. [41] developed a unified plastic creep constitutive model to characterize the plasticity and hardening behavior of solder. In this preliminary study, we focused on verifying the feasibility of the coupling algorithm for package structure analysis. Therefore, we simplified the model by considering only elastic material behavior.

4.1. Multilayered structure incorporating sintered silver

Consider a 2D SiC chip model with dimensions $a \times c$, connected to a Cu substrate through sintered silver technology. The length of the SiC chip $a = 1.8$ mm, height $c = 0.5$ mm, the thickness of the sintered

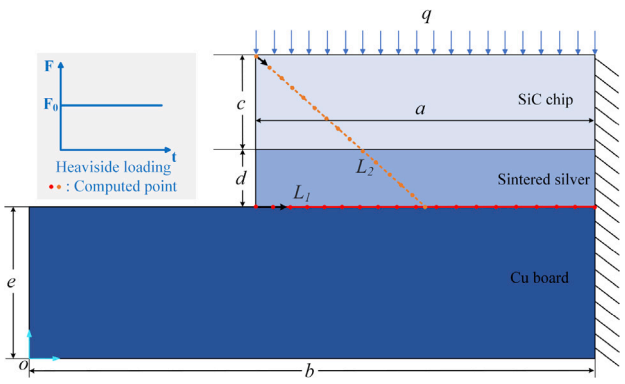

Fig. 4. Sintered silver structure model.

Table 1
Material parameters used in the model.

Material	Density ρ (t/mm^3)	Young's modulus E (MPa)	Poisson's ratio υ
SiC chip	3.2	430,000	0.17
Sintered silver	10.49	12,900	0.10
Cu board	8.96	99,800	0.34

silver interconnect layer $d = 0.3$ mm (with the same length as the SiC chip), Cu substrate length $b = 3.0$ mm, height $e = 0.8$ mm, and the material parameters for the model can be referred to in Table 1. As depicted in Fig. 4, the upper side of the model is subjected to a uniformly distributed load in the y-direction, with a magnitude of $q = 1$ N/mm, applied as a Heaviside step loading. The right end of the model is fixed, with $u_x = 0$ and $u_y = 0$ imposed as boundary conditions.

In this model, the finite element domain consists of the SiC chip and the sintered silver layer, while the boundary element domain includes the Cu substrate. The finite element region is discretized using quadrilateral structured elements, and the boundary element region employs linear boundary elements. Fig. 5 shows the meshes used in the numerical model. For the analysis, initially, two model components are initially constructed within the Abaqus platform: the finite element part and the equivalent boundary element part. Subsequently, the connection between these two models is established using the 'tie' command available in Abaqus.

To illustrate the accuracy of this coupling algorithm, a finite element model was constructed using the commercial software Abaqus, and the results obtained with a highly refined mesh were employed as a reference solution. Figs. 6(a) and 6(b) display the stress distribution within the SiC chip at $t = 0.05$ s, obtained using the coupled scheme and the reference solution, respectively. As evident from these figures, the results derived from the coupling method exhibit overall good agreement with the reference solution. Given that the contact interface between FE and BE domains represents a critical area, Figs. 7(a) and 7(b) present stress contours of the sintered silver region to demonstrate consistency between our results and the reference solution.

To further validate the computational accuracy of the coupling algorithm, we define the red solid line (representing the contact interface) as L_1 and the orange dashed line in Fig. 4 as L_2. As shown in Fig. 4, calculation points are marked along two lines, with black arrows indicating sampling directions. The equations for L_1 and L_2 can be expressed as:

$$L_1 = \{(x, y) : b - a \le x \le b, y = e\} \tag{47}$$

$$L_2 = \{(x, y) : b - a \le x \le b - a/2, e \le y \le c + d + e\} \tag{48}$$

Figs. 8 and 9 respectively show the comparison of the numerical solutions for displacements U along lines L_1 and L_2, calculated by the

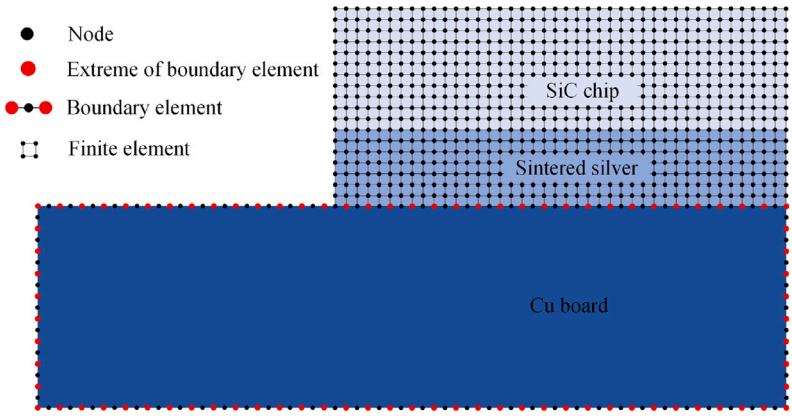

Fig. 5. Schematic of the mesh employed in the finite element–boundary element coupling scheme.

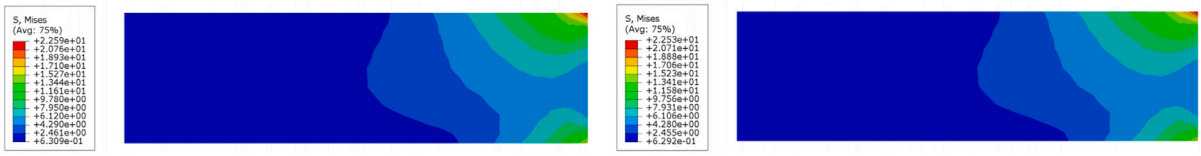

(a) Results obtained by coupling scheme. (b) Reference results obtained by a very refined FEM model.

Fig. 6. von Mises stress (MPa) distribution of SiC chip obtained by two methods at $t = 0.05$ s.

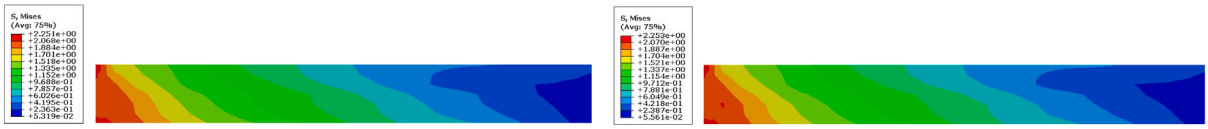

(a) Present coupling method (b) Reference solution

Fig. 7. von Mises stress contours (MPa) of sintered silver region at $t = 0.02$ s: (a) present coupling method; (b) reference solution.

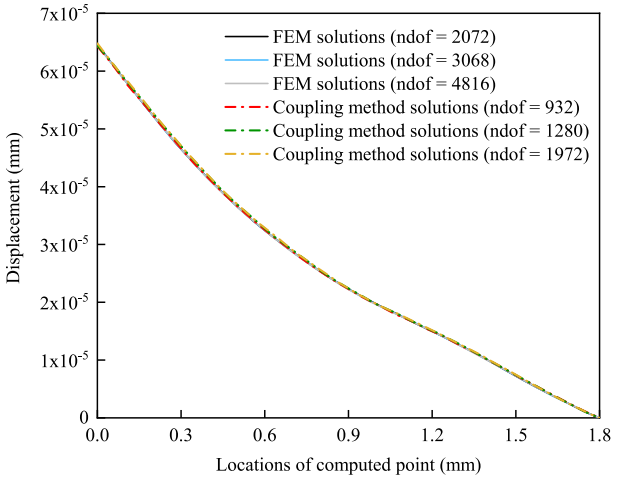

Fig. 8. Displacements U along the line L_1 obtained by the different methods at $t = 0.12$ s.

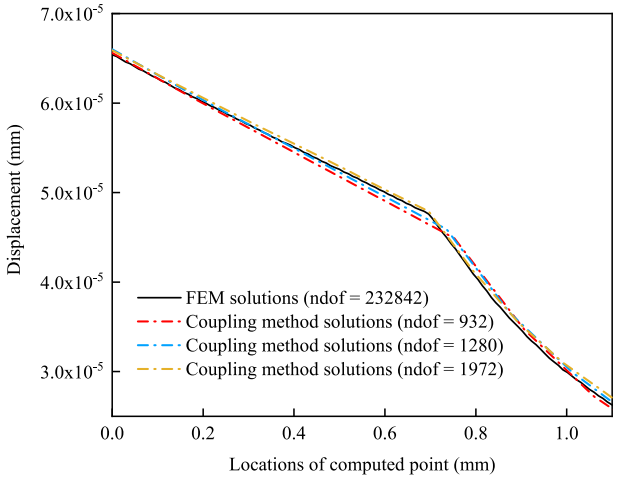

Fig. 9. Displacements U along the line L_2 obtained by the different methods at $t = 0.12$ s.

proposed coupling algorithm and the finite element method (Abaqus) with varying degrees of freedom at $t = 0.12$ s. The displacement is defined as $U = \sqrt{u_1^2 + u_2^2}$, with u_1 and u_2 being the x- and y-directional displacements. It can be seen from the figures that the results obtained by the coupling method along line L_1 exhibit good agreement with the reference solutions from the finite element method, demonstrating consistent behavior. Furthermore, the results presented in Fig. 9 reveal that as the degree of freedom increases, the solutions obtained through

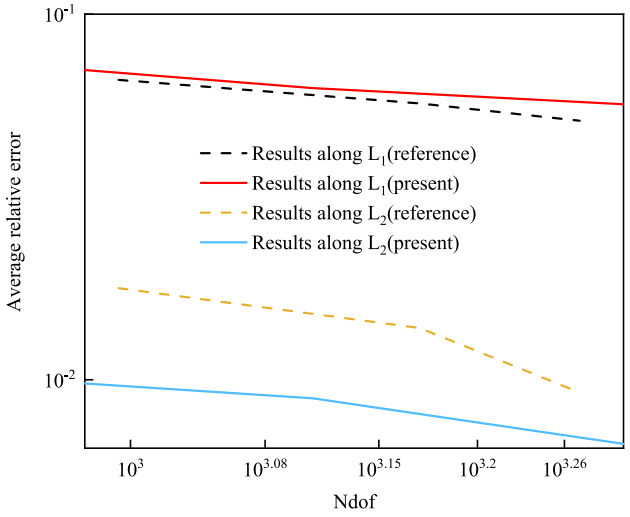

Fig. 10. Convergence curves of displacements U obtained by using different methods.

the coupling scheme converge towards the reference solution. This convergence behavior further corroborates the correctness and reliability of the proposed coupling algorithm.

To further verify the convergence of the coupling algorithm, an average relative error is defined, and its expression is:

$$\text{Average relative error(ARE)} = \frac{1}{N}\sum_{n=1}^{N}\left|\frac{U_n - U_{ref}}{U_{ref}}\right| \tag{49}$$

where N is the number of nodes used in the calculation; U_n is the displacement of the nth node; U_{ref} is the reference displacement value of the corresponding node.

Fig. 10 illustrates the average relative errors in the displacement solutions along lines L_1 and L_2 as a function of the degree of freedom at $t = 0.12$ s. In this comparison, the reference solutions are obtained from a highly refined finite element model with 232,842 degrees of freedom.

4.2. Dynamic response of TGV-Cu structure

In the second numerical example, the coupling algorithm is employed to analyze the transient behavior of a TGV-Cu (Through Glass Via-Copper) structure. TGV is a vertical electrical interconnection technology that passes through a glass substrate and is typically filled with copper (Cu). Fig. 11 illustrates the simplified model of the TGV-Cu structure studied in this numerical example. In the model, the depth of the TGV-Cu is $b = 100$ μm, the width is $c = 10$ μm, the thickness of the copper covering layer is 10 μm, and the geometric dimensions of the glass part are $a = 630$ μm and $d = 250$ μm. The boundary conditions are as follows: the bottom of the glass substrate is fixed ($u_x = u_y = 0$), and Heaviside step function shear load in the x-direction, with a magnitude of $t = 250$ N/mm, is applied to the upper surface of the Cu covering layer. The material parameters of the model are listed in Table 2.

Table 2
Material parameters used in the computation.

Material	Density ρ (T/mm^3)	Young's modulus E (MPa)	Poisson's ratio υ
Cu	8.9	155,000	0.3
Glass	2.51	77,000	0.24

Since the size of the glass substrate is significantly larger than that of the Cu component, the FEM is employed to analyze the Cu, while the BEM is utilized for the glass substrate, thereby reducing the number of elements required for the analysis. This approach requires discretizing only the boundary of the glass substrate. Fig. 12 shows the schematic diagram of meshes used in the coupling scheme. In the finite element region, quadratic quadrilateral meshes are used, while in the boundary element region, quadratic linear elements are employed for discretization.

Fig. 13 compares the displacement results computed by both methods at $t = 2$ s. The results show strong agreement between the coupling method and FEM at the interface, despite the coupling algorithm using significantly fewer degrees of freedom (ndof = 218). This demonstrates the coupling algorithm's ability to maintain stability even with a reduced number of degrees of freedom. Table 3 presents detailed computational results at each point for varying degrees of freedom, using the refined-mesh FEM results as a reference solution. The data reveals that as the number of degrees of freedom increases, the coupling algorithm's results progressively converge towards the FEM solutions.

Define line L_2, located as shown in Fig. 11. The figure illustrates both the calculation point positions and their sampling directions, indicated by green and gray arrows. Its parametric equation can be expressed as:

$$L_2 = \{(x, y) : x = a/2, d - b \le y \le c + d\} \tag{50}$$

Fig. 14 displays the displacement values at various points on line L_2 under different degrees of freedom, obtained using the coupling method. For comparison, the reference solution derived from the FEM is also provided. The diagram shows that the results calculated by the coupling method are in good agreement with those of the reference method, further verifying the precision and accuracy of this method.

To further verify the stability of the computational results of the coupling algorithm, we selected three points A, B, and C within the finite element domain, as shown in Fig. 12. Figs. 15(a) and 15(b) show the stress and displacement curves over time at points A, B, and C,

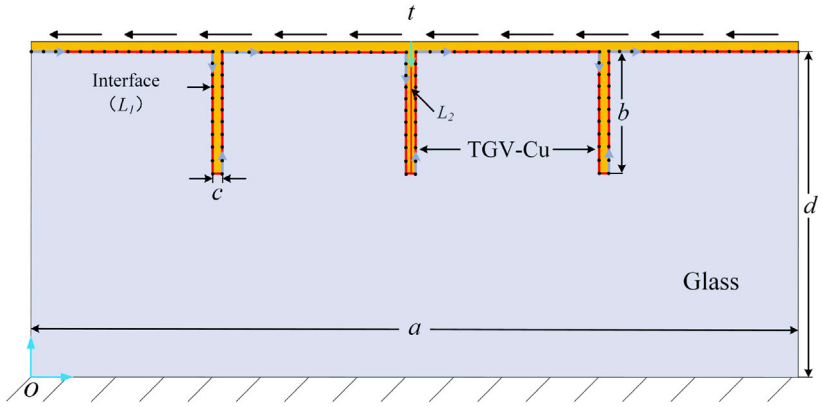

Fig. 11. The considered TGV-Cu structure model. (For interpretation of the references to color in this figure legend, the reader is referred to the web version of this article.)

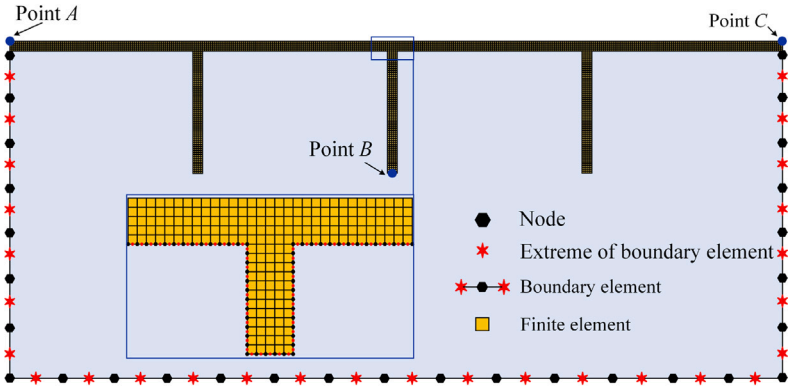

Fig. 12. Schematic diagram of meshes used in the coupling scheme for the TGV-Cu structure.

Table 3
The numerical and reference solutions of displacements U on the contact interface at $t = 2$ s.

Locations of computed point on the interface (mm)	Numerical results ($\times 10^{-3}$)			Reference results ($\times 10^{-3}$)
	ndofs = 218	ndofs = 326	ndofs = 768	ndofs = 41,012
0	3.981	3.938	3.853	3.811
0.15	3.014	3.004	2.989	2.990
0.2	2.375	2.365	2.355	2.331
0.25	1.750	1.747	1.741	1.680
0.26	1.739	1.737	1.732	1.672
0.31	2.358	2.352	2.342	2.318
0.36	2.990	2.980	2.965	2.965
0.51	2.793	2.786	2.776	2.752
0.56	2.282	2.275	2.266	2.228
0.61	1.736	1.732	1.726	1.665
0.67	2.282	2.275	2.266	2.228
0.72	2.793	2.786	2.776	2.752
0.87	2.990	2.980	2.965	2.965
0.92	2.358	2.352	2.342	2.318
0.97	1.739	1.737	1.732	1.672
0.98	1.750	1.747	1.741	1.680
1.03	2.375	2.365	2.355	2.331
1.08	3.014	3.004	2.989	2.990
1.23	3.981	3.938	3.853	3.811

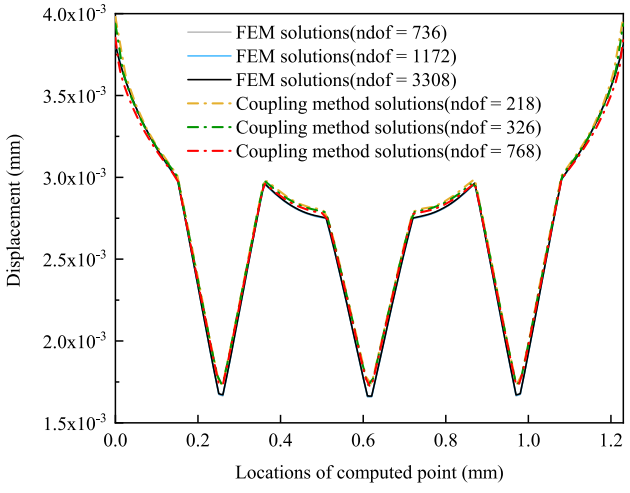

Fig. 13. Displacement U distribution at the coupling interface of the TGV-Cu model at $t = 2$ s.

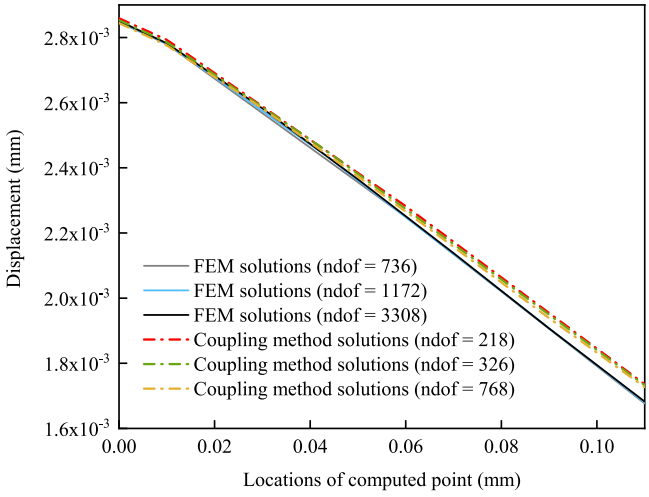

Fig. 14. Displacement U distribution along L_2 at the contact interface of the TGV-Cu model at $t = 2$ s.

respectively. As observed, due to the symmetry of the structure, the stress and displacement curves at points A and C coincide completely. As time progresses, the computational results from both methods tend to stabilize, and the obtained results match very well. Notably, the coupling algorithm not only maintains high accuracy but also stabilizes more quickly.

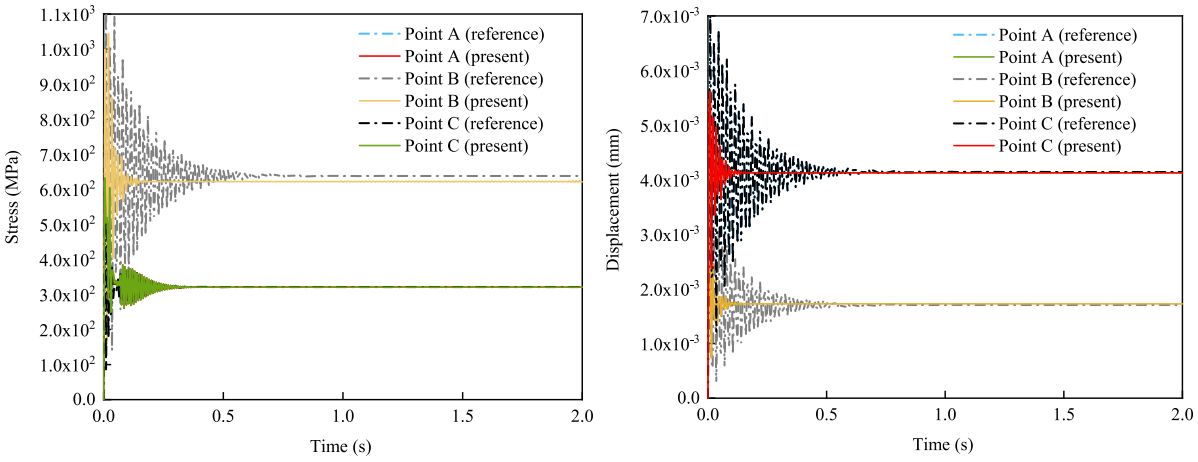

(a) von Mises stress results. (b) Displacement U results.

Fig. 15. Numerical results obtained by different methods at points A, B, and C.

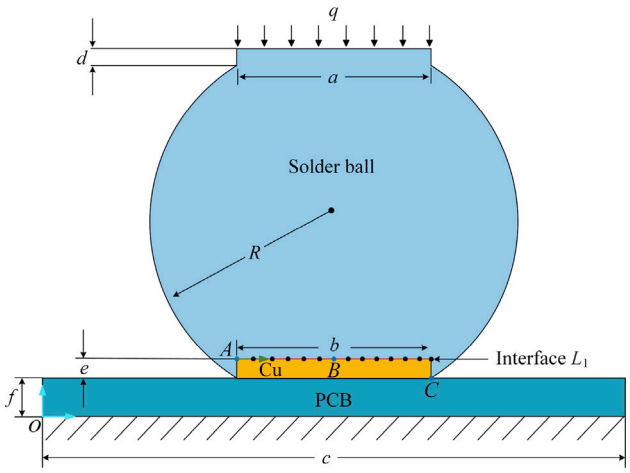

Fig. 16. The considered BGA solder ball model. (For interpretation of the references to color in this figure legend, the reader is referred to the web version of this article.)

Table 4
Material parameters used in the numerical model.

Material	Density ρ (T/mm^3)	Young's modulus E (MPa)	Poisson's ratio υ
BGA	7.3	10 000	0.4
Cu	8.9	110 000	0.35
PCB	2.1	22 000	0.15

4.3. Dynamics response of BGA solder ball structure

Here, a portion of the solder ball structure in a Ball Grid Array (BGA) is selected for dynamic analysis. As shown in Fig. 16, the model comprises solder balls, a copper layer, and a PCB substrate. The geometric parameters of the model are $a = b = 1$ mm, $c = 3$ mm, $d = e = 0.05$ mm, $f = 0.2$ mm, $R = 0.94$ mm. Table 4 provides the material parameters employed. A uniform load is applied along the y-direction on the upper surface of the solder ball, with the lower end of the PCB board fixed. This example considers two types of loading as shown in Fig. 17: a unit step function load and a linear function load, both with a maximum load $F_0 = 10$ N/mm.

In the coupling algorithm, the FEM is employed to analyze the PCB substrate and copper layer components, while the BEM is utilized for the solder ball part. The meshes used in the coupling algorithm and the conventional FEM are depicted in Figs. 18(a) and 18(b), respectively. It is evident that in the coupling approach, only the boundary of the solder ball part requires discretization, significantly reducing the total number of mesh elements in comparison to the finite element method. The FE domain is discretized using 4-node quadrilateral elements (CPE8R), while quadratic elements are used for the discretization of the BE domain.

Firstly, a unit Heaviside loading is applied to the model. Fig. 19 illustrates the displacement results along the contact interface L_1 at $t = 0.12$ s, obtained using the coupling algorithm and the reference method, respectively. The calculation points along L_1 are shown as black dots in Fig. 16, with green arrows indicating their corresponding sampling directions. Fig. 20 presents the stress distribution within the copper layer and PCB substrate at that instant, as computed using the coupling method and the reference method. As shown in the figures, there are some differences in the results. These can be attributed to the sudden application of unit step loading and the presence of corner points in the geometric model, leading to stress jumps and numerical fluctuations. When using the FEM, mesh refinement is a possible solution. However, due to the singularities at corner points, obtaining accurate physical quantities remains challenging. The BEM offers advantages for such regions due to its singular fundamental solutions. The differences between our coupling method and reference solutions are relatively small, consistent with similar studies [42]. In this preliminary study, we focused on verifying the feasibility of the coupling algorithm for packaging structure dynamics. Future work will apply this method to more specialized models to fully utilize its advantages.

To further validate the computational results obtained via the coupling method, three points A, B, and C were selected along the contact interface, with their locations depicted in Fig. 16. Fig. 21 illustrates the temporal evolution of displacement U at points A and B, calculated using the coupling method with varying degrees of freedom under Heaviside loading case. The reference solution obtained from the finite element model is also provided in the figure for comparison purposes. As evident from the figure, the computational results of the coupling algorithm exhibit stable behavior across different degrees of freedom.

Fig. 22 depicts the displacements at various points along the contact interface L_1 at $t = 0.12$ s, calculated using the coupling algorithm with different degrees of freedom under a linear function load condition. It can be observed that the numerical solutions obtained through the coupling algorithm exhibit good agreement with the reference solutions.

Figs. 23(a) and 23(b) illustrates the temporal evolution of displacement at points B and C (with locations shown in Fig. 16). The figure demonstrates that the computational results of the coupling algorithm

(a) Heaviside loading. (b) Linear loading.

Fig. 17. Types of loading used in the model.

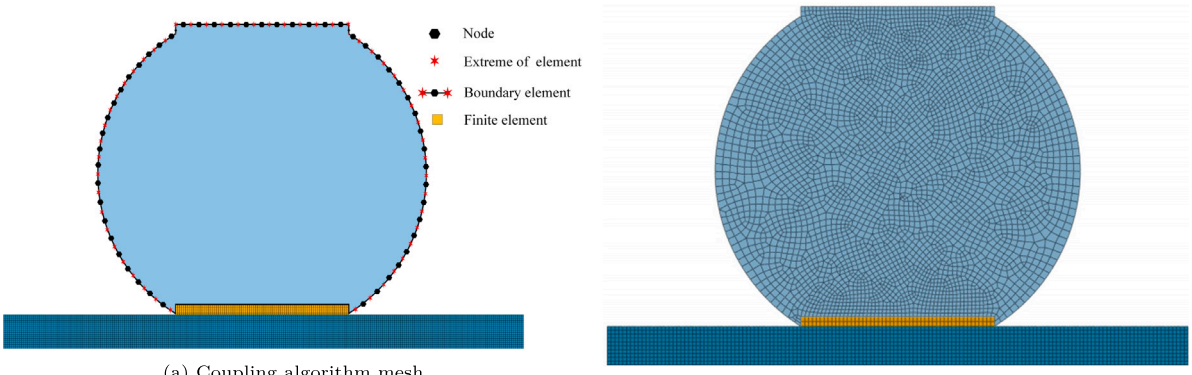

(a) Coupling algorithm mesh. (b) Reference solution mesh.

Fig. 18. Meshes used in the numerical analysis.

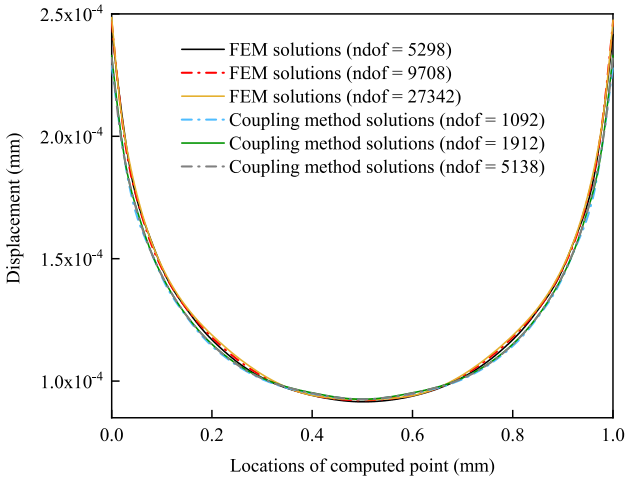

Fig. 19. Displacement U on contact interface under Heaviside loading.

converge under varying degrees of freedom and align well with the results calculated using the reference method.

Here, we analyze the computational efficiency of the proposed coupling scheme. The efficiency advantages of FE–BEM coupling are context-dependent and particularly related to the BEM application domain. While the BEM coefficient matrix is non-symmetric and full-rank, this method effectively reduces the model's degrees of freedom (dof) during analysis. A key advantage of BEM is that its coefficient matrix depends solely on the geometric boundary and its discretization. This means that once the BEM coefficient matrix is computed, subsequent modifications to the FE region (such as mesh refinement) do not require recalculation of BEM coefficients — these can be reused, leading to significant computational savings.

To quantitatively evaluate the computational efficiency, we compared the computational times for different degrees of freedom under two loading conditions. The results were benchmarked against Abaqus finite element analyses using identical element sizes for the Cu and PCB regions, while only varying the mesh density in the solder ball region. As shown in Table 5, the present coupling method achieves shorter computation times while maintaining solution accuracy for electronic packaging elastodynamics problems, demonstrating improved computational efficiency.

5. Conclusions

This article presents a finite element–boundary element coupling algorithm tailored for solving transient elastic dynamic response problems in electronic packaging structures, effectively leveraging the advantages offered by both methodologies. In the numerical implementation, the model is partitioned into finite element and boundary element domains based on the geometric characteristics or material properties, with each domain solved using the respective finite element and boundary element methods. Notably, the boundary element domain is treated as a specialized finite element, wherein a self-written boundary element program is invoked through the user-defined element (UEL) subroutine to obtain its equivalent stiffness and load representations. These are subsequently utilized as prescribed boundary conditions to determine the unknown quantities within the finite element domain. Numerical examples validate the accuracy and effectiveness of this coupling approach in analyzing transient dynamic response problems pertinent to electronic packaging structures. The current method, while effective for the presented cases, has several limitations that warrant further development. First, the current implementation is limited to elastic material behavior, which may not fully capture the complex mechanical response of electronic packaging materials under dynamic loading. Second, the method is currently restricted to 2D problems. To address these limitations, our future work will focus on: Incorporating

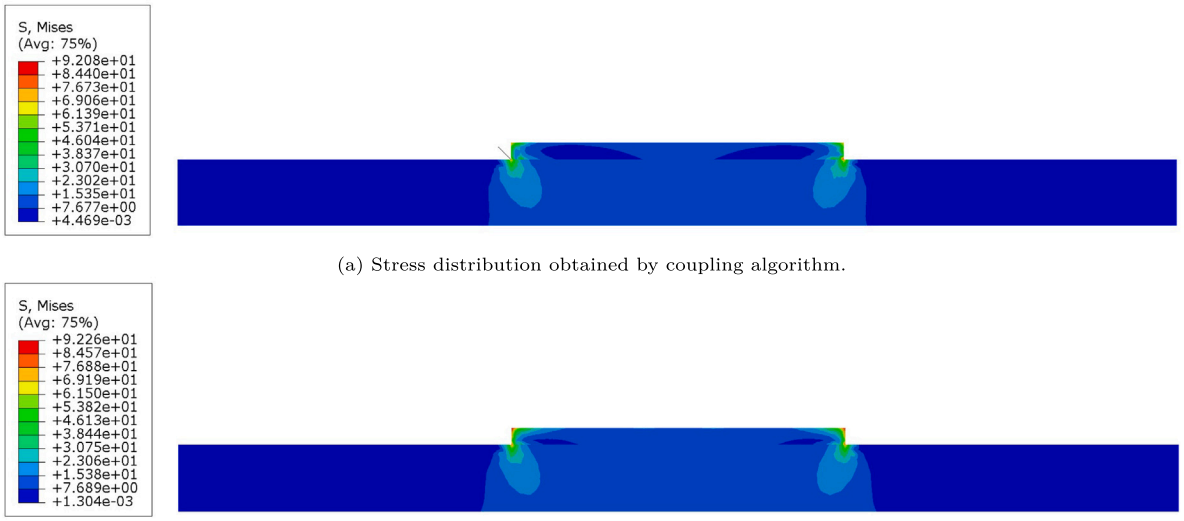

(a) Stress distribution obtained by coupling algorithm.

(b) Stress distribution obtained by FEM model with fined meshes.

Fig. 20. von Mises stress (MPa) distribution at $t = 0.12$ s under Heaviside loading.

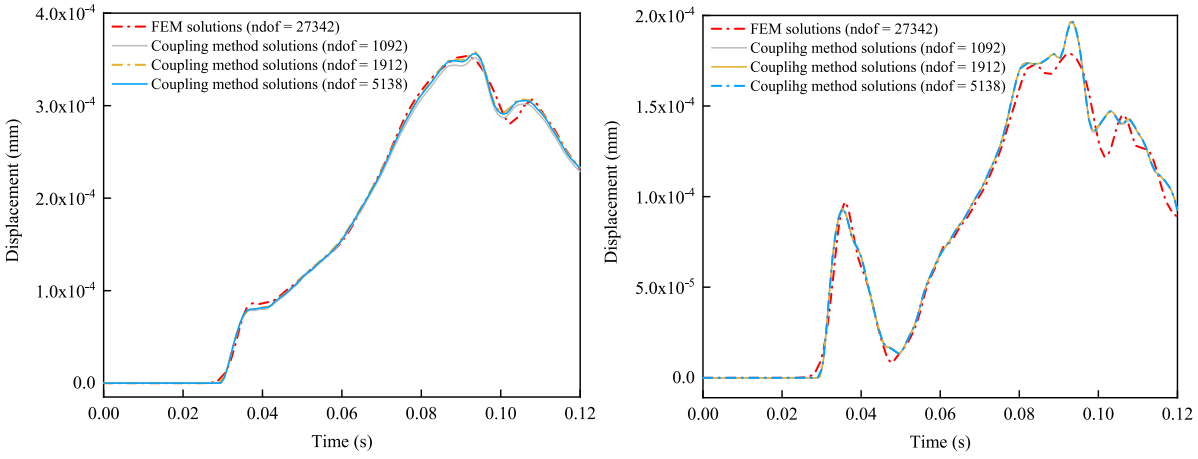

(a) Displacement at point A.

(b) Displacement at point B.

Fig. 21. Displacements U over time at points A and B when $t = 0.12$ s under Heaviside loading case.

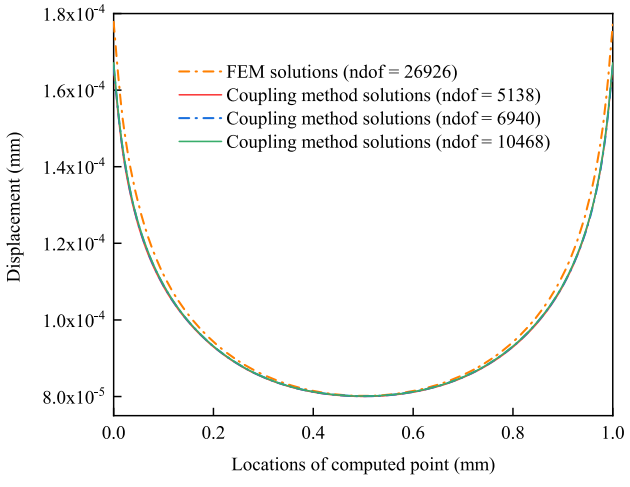

Fig. 22. Displacements U on contact interface L_1 under linear loading.

elastoplastic constitutive models to better represent material behavior;and Extending the method to three-dimensional problems to handle more realistic packaging configurations.

CRediT authorship contribution statement

Yanpeng Gong: Writing – review & editing, Writing – original draft, Supervision, Software, Methodology, Funding acquisition. **Yida He:** Visualization, Validation. **Han Hu:** Supervision. **Xiaoying Zhuang:** Supervision. **Fei Qin:** Supervision. **Hao Xu:** Validation. **Timon Rabczuk:** Supervision.

Declaration of competing interest

The authors declare that they have no known competing financial interests or personal relationships that could have appeared to influence the work reported in this paper.

Acknowledgments

The authors acknowledge the support from the National Natural Science Foundation of China (No. 12002009) and the Alexander von Humboldt Foundation, Germany.

Data availability

Data will be made available on request.

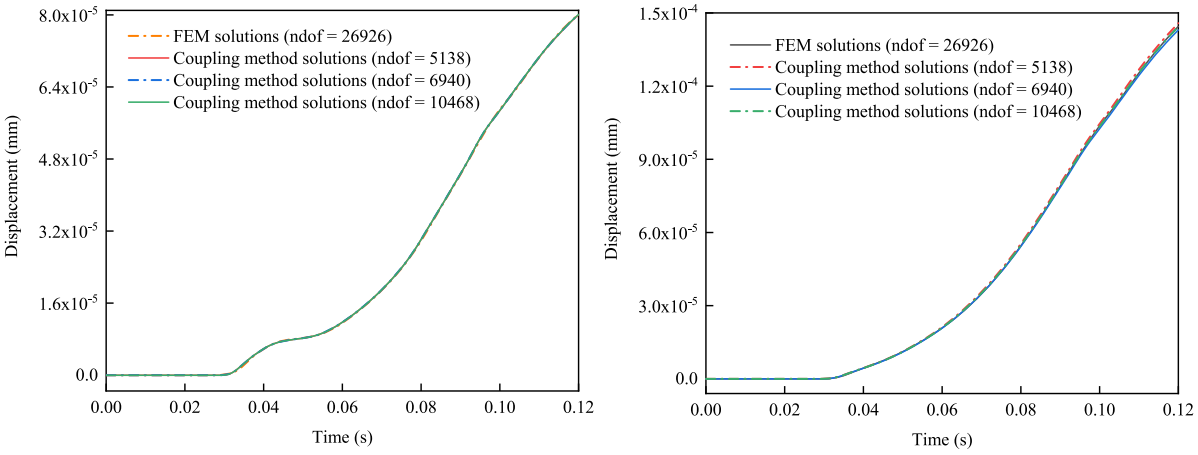

(a) Displacement at point B. (b) Displacement at point C.

Fig. 23. Displacements U over time at points B and C when $t = 0.12$ s under linear loading case.

Table 5
Comparisons of computation for different methods under different loadings.

Methods	ndof	Heaviside loading			Linear loading		
		CPU (s)	Wall time (s)	U at point B	CPU (s)	Wall time (s)	U at point B
FEM	11 970	0.5	1	9.22541e−5	0.5	1	8.00211e−5
	21 442	0.6	1	9.21083e−5	0.6	1	8.00786e−5
	47 230	1.5	1	9.215e−5	1.4	2	8.01611e−5
Coupled	1092	0.3	1	9.23872e−5	0.2	1	7.9945e−5
	1912	0.3	1	9.25222e−5	0.3	1	8.00323e−5
	5138	0.4	1	9.25145e−5	0.5	1	8.00221e−5

References

[1] Saravanakumar K, Saravanan S, Muthuram N. Investigation of dynamic characteristics and fatigue life prediction of Pb free solder material under random vibration. Mater Res Express 2024;11(8):086301.

[2] Quinones H, Babiarz A. Chip scale packaging reliability. In: International symposium on electronic materials and packaging (EMAP2000) (cat. no.00EX458). 2000, p. 398–405.

[3] Karpik A, Cosco F, Mundo D. Higher-order hexahedral finite elements for structural dynamics: A comparative review. Machines 2023;11(3).

[4] Barros G, Pereira A, Rojek J, Carter J, Thoeni K. Efficient multi-scale staggered coupling of discrete and boundary element methods for dynamic problems. Comput Methods Appl Mech Engrg 2023;415:116227.

[5] Liew K, He X, Tan M, Lim H. Dynamic analysis of laminated composite plates with piezoelectric sensor/actuator patches using the FSDT mesh-free method. Int J Mech Sci 2004;46(3):411–31.

[6] Gu Y, Qu W, Chen W, Song L, Zhang C. The generalized finite difference method for long-time dynamic modeling of three-dimensional coupled thermoelasticity problems. J Comput Phys 2019;384:42–59.

[7] Yahiaoui H, Lakis A, Toorani M. Hybrid finite element theory in dynamic analysis of an imperfect plate. Mech Res Commun 2024;141:104324.

[8] Chen L, Wang Z, Lian H, Ma Y, Meng Z, Li P, et al. Reduced order isogeometric boundary element methods for CAD-integrated shape optimization in electromagnetic scattering. Comput Methods Appl Mech Engrg 2024;419:116654.

[9] Omar A, Sitli Y, Elmhaia O, Rammane M, Mesmoudi S, Hilali Y, et al. Impact of polymeric composites on static and dynamic behaviors of timoshenko beams using spectral and newmark-β methods. J Vib Eng Technol 2024;1–26.

[10] Jamali HU, Tolephih MH, Jweeg MJ, Aljibori H, Mohammed M, Abdullah OI, et al. Analysis of the dynamic response of variable bearing design under impact load using taguchi method. In: International tribology symposium of IFToMM. Springer; 2024, p. 202–12.

[11] Xia J, Cheng L, Li G, Li B. Reliability study of package-on-package stacking assembly under vibration loading. Microelectron Reliabil 2017;78:285–93.

[12] Kim YK, min Lee S, soon Hwang D, Jang S. Analyses on the large size PBGA packaging reliability under random vibrations for space applications. Microelectron Reliabil 2020;109:113654.

[13] Agwai A, Guven I, Madenci E. Damage prediction for electronic package drop test using finite element method and peridynamic theory. In: 2009 59th electronic components and technology conference. 2009, p. 565–9.

[14] Zhang B, kuan Liu P, Ding H, Cao W. Modeling of board-level package by finite element analysis and laser interferometer measurements. Microelectron Reliabil 2010;50(7):1021–7, Thermal, Mechanical and Multi-physics Simulation and Experiments in Micro-Electronics and Micro-Systems (EuroSimE 2009).

[15] Venkata Naga Chandana Y, Venu Kumar N. Drop test analysis of ball grid array package using finite element methods. Mater Today: Proc 2022;64:675–9, International Conference on Advanced Materials for Innovation and Sustainability.

[16] Gong W, Huang M, Chen L, Tang L, Ye L. Dynamic characteristics analysis of the flip chip bonding head based on multiple working conditions. In: 2013 14th international conference on electronic packaging technology. 2013, p. 732–7.

[17] Jia Y, Xiao F, Duan Y, Luo Y, Liu B, Huang Y. PSpice-COMSOL-based 3-D electrothermal–mechanical modeling of IGBT power module. IEEE J Emerg Selected Top Power Electron 2020;8(4):4173–85.

[18] Tay AAO, Lee KH, Lim KM. Numerical simulation of delamination in IC packages using a new variable-order singular boundary element. J Electron Packaging 2003;125(4):569–75.

[19] Khatir Z, Lefebvre S. Boundary element analysis of thermal fatigue effects on high power IGBT modules. Microelectron Reliabil 2004;44(6):929–38.

[20] Dong C, Lee KY. Stress analysis of plastic IC package containing various interface delaminations using the boundary element method. Eng Fract Mech 2008;75(1):1–16.

[21] Yu H, Guo Y, Gong Y, Qin F. Thermal analysis of electronic packaging structure using isogeometric boundary element method. Eng Anal Bound Elem 2021;128:195–202.

[22] Gong Y, Trevelyan J, Hattori G, Dong C. Hybrid nearly singular integration for isogeometric boundary element analysis of coatings and other thin 2D structures. Comput Methods Appl Mech Engrg 2019;346:642–73.

[23] Gong Y, Dong C, Qin F, Hattori G, Trevelyan J. Hybrid nearly singular integration for three-dimensional isogeometric boundary element analysis of coatings and other thin structures. Comput Methods Appl Mech Engrg 2020;367.

[24] Gong Y, Qin F, Dong C, Trevelyan J. An isogeometric boundary element method for heat transfer problems of multiscale structures in electronic packaging with arbitrary heat sources. Appl Math Model 2022;109:161–85.

[25] Zienkiewicz OC, Taylor RL. The finite element method for solid and structural mechanics. Elsevier; 2005.

[26] Gernot Beer CD. The boundary element method with programming. first ed.. (1). Springer Vienna; 2008.

[27] Guven I, Madenci E, Chan CL. Transient two-dimensional heat conduction analysis of electronic packages by coupled boundary and finite element methods. IEEE Trans Components Packaging Technol 2002;25(4):684–94.

[28] Das M, Guven I, Madenci E. Coupled BEM and FEM analysis of functionally graded material layers. J Therm Stresses 2006;29(3):263–87.
[29] Qin F, He Q, Gong Y, Hou C, Cheng H, An T, et al. An automatic finite element method-boundary element method coupling method for elastic–plastic problems of multiscale structures in electronic packaging. J Electron Packaging 2023;145(2).
[30] Qin F, He Q, Gong Y, An T, Chen P, Dai Y. The application of FEM-BEM coupling method for steady 2D heat transfer problems with multi-scale structure. Eng Anal Bound Elem 2022;137:78–90.
[31] Chen L, Lian H, Pei Q, Meng Z, Jiang S, Dong H-W, et al. FEM-BEM analysis of acoustic interaction with submerged thin-shell structures under seabed reflection conditions. Ocean Eng 2024;309:118554.
[32] Chen L, Lian H, Dong H-W, Yu P, Jiang S, Bordas SP. Broadband topology optimization of three-dimensional structural-acoustic interaction with reduced order isogeometric FEM/BEM. J Comput Phys 2024;509:113051.
[33] Ji D, Lei W, Liu Z. Finite element method and boundary element method iterative coupling algorithm for 2-D elastodynamic analysis. Comput Appl Math 2020;39(3):218.
[34] Genes MC, Kocak S. Dynamic soil–structure interaction analysis of layered unbounded media via a coupled finite element/boundary element/scaled boundary finite element model. Internat J Numer Methods Engrg 2005;62(6):798–823.
[35] Genes MC. Dynamic analysis of large-scale SSI systems for layered unbounded media via a parallelized coupled finite-element/boundary-element/scaled boundary finite-element model. Eng Anal Bound Elem 2012;36(5):845–57.
[36] Liu Z, Dong C. Automatic coupling of ABAQUS and a boundary element code for dynamic elastoplastic problems. Eng Anal Bound Elem 2016;65:147–58.
[37] Dominguez J. Boundary elements in dynamics. Wit Press; 1993.
[38] Long X, Dong R, Shi H, Huang T, Shao Z, Su Y. Strain rate effect on indentation behavior of polycrystalline sintered silver nanoparticles based on crystal plasticity finite element method. In: 2024 25th international conference on electronic packaging technology. ICEPT, IEEE; 2024, p. 1–6.
[39] Mao M, Wang W, Lu C, Jia F, Long X. Machine learning for board-level drop response of BGA packaging structure. Microelectron Reliabil 2022;134:114553.
[40] Long X, Chen Z, Wang W, Fu Y, Wu Y. Parameterized Anand constitutive model under a wide range of temperature and strain rate: experimental and theoretical studies. J Mater Sci 2020;55(24):10811–23.
[41] Wang W, Long X, Du C, Fu Y, Yao Y, Wu Y. Enhancement of the unified constitutive model for viscoplastic solders in wide strain rate and temperature ranges. Strength Mater 2019;51:917–25.
[42] Chien C-C, Wu T-Y. A particular integral BEM/time-discontinuous FEM methodology for solving 2-D elastodynamic problems. Int J Solids Struct 2001;38(2):289–306.